International Journal of Heat and Fluid Flow 116 (2025) 109862

Contents lists available at ScienceDirect

International Journal of Heat and Fluid Flow

journal homepage: www.elsevier.com/locate/ijhff

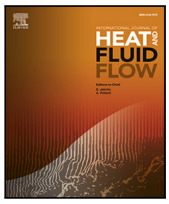

Restricted nonlinear simulations of flow over riblets: Characterizing drag reduction and its breakdown

Xiaowei Zhu [a], Bianca Viggiano [b,*], Benjamin A. Minnick [c], Dennice F. Gayme [d]

[a] Department of Mechanical and Material Engineering, Portland State University, 1825 SW Broadway, Portland, 97201, OR, USA
[b] Department of Mechanical Engineering, Polytechnique Montréal, 2500 Chem. de Polytechnique, Montréal, H3T 1J4, QC, Canada
[c] Submarine Maneuvering and Control Division, Naval Surface Warfare Center Carderock Division, 9500 MacArthur Blvd, West Bethesda, 20817, MD, USA
[d] Department of Mechanical Engineering, Johns Hopkins University, 3400 N Charles St, Baltimore, 21218, MD, USA

ARTICLE INFO

Dataset link: https://github.com/lesgo-jhu/lesgo

Keywords:
Restricted nonlinear modeling
Riblets
Turbulent structures
Drag reduction

ABSTRACT

The restricted nonlinear (RNL) model is employed as low-order representation of turbulent flow over riblets at $Re_\tau \approx 395$. Comparisons with direct numerical simulations (DNS) verify the ability of the model to accurately capture low-order statistics, as well as trends in drag-alteration and secondary motion as a function of riblet geometry and spacing. We demonstrate the ability of the RNL model to reproduce additional flow features by decomposing the roughness function to isolate contributions from the total stress and comparing its predictions to DNS data. An analysis of the spectra of Reynolds shear stress shows that the RNL model captures Kelvin-Helmholtz-like rollers linked to riblet drag reduction breakdown but slightly over predicts the total stresses. The reproduction of the overall trends in stresses and flow features linked to the breakdown of riblet induced drag-reduction suggests that the nonlinearity and scale interactions retained in the RNL system are adequate to capture the key mechanisms underlying turbulent flow over a range of riblet geometries. These results also indicate that examining the limitations of the model may provide insight into the critical nonlinear interactions underlying drag alteration due to riblets.

1. Introduction

Friction drag is responsible for a significant portion of transport efficiency loss in a range of applications (Zheng and Yan, 2010; Jo et al., 2018; Gómez-de Segura and García-Mayoral, 2019). Identifying effective methods to reduce turbulent drag is therefore both a critical and a practical challenge, with implications for various engineering applications, including minimizing drag on ship hulls and airplane wings. One promising approach is surface modification through the introduction of spanwise-varying micro-grooves that are commonly referred to as riblets (Kramer, 1937; Walsh, 1980, 1982; Walsh and Lindemann, 1984; Goldstein et al., 1995). Riblets have been shown to reduce friction drag up to 10% compared to flow over a smooth surface at low to moderate Reynolds numbers (Bechert et al., 1997; García-Mayoral and Jiménez, 2011a; Wen et al., 2020; Modesti et al., 2021; Rouhi et al., 2022; Wong et al., 2024). Numerous studies have demonstrated that the characteristic length scale for a given riblet geometry greatly impacts the friction drag over the riblet surface (Walsh, 1980; Walsh and Lindemann, 1984; Bechert and Bartenwerfer, 1989; Luchini et al., 1991; Bechert et al., 1997, 2000; García-Mayoral and Jiménez, 2011a,b). This length scale can be defined in terms of the riblet spacing (Bechert and Bartenwerfer, 1989; Choi et al., 1993), or the square root of the area between adjacent riblets (García-Mayoral and Jiménez, 2011b). In the viscous regime, narrowly spaced riblets reduce friction drag and this reduction in drag continues to grow with increases in the characteristic length-scale until minimum friction drag is achieved (Garcia-Mayoral et al., 2019; García-Mayoral and Jiménez, 2011b). Beyond the minimum drag point, increasing the riblet spacing leads to progressively less drag reduction until the spacing becomes large enough that riblet-lined walls cause a higher frictional drag than the corresponding smooth wall (García-Mayoral and Jiménez, 2011b, 2012; Newton et al., 2018).

Exploiting the full potential of riblets as a passive drag-reduction technique requires an in-depth understanding of the full range of mechanisms governing both drag reduction and its breakdown across the full range of potential geometries and flow regimes. Numerical studies of riblets face significant challenges. Resolving turbulent flow interactions with riblets whose length scales are on the order of single-digit wall units (Bechert and Bartenwerfer, 1989; Luchini et al., 1991; Choi et al., 1993) requires spanwise (z direction) resolution on the

* Corresponding author.
E-mail address: bianca.viggiano@polymtl.ca (B. Viggiano).

https://doi.org/10.1016/j.ijheatfluidflow.2025.109862
Received 6 February 2025; Received in revised form 19 April 2025; Accepted 20 April 2025
Available online 27 May 2025

order of $\Delta z^+ \sim \mathcal{O}(1)$ (Choi et al., 1993; Goldstein et al., 1995; Goldstein and Tuan, 1998; García-Mayoral and Jiménez, 2011a). Here the superscript "+" indicates quantities in wall units, i.e., normalized by the friction velocity u_τ and the viscosity ν. In contrast, DNS of flow over smooth walls under similar conditions typically employ $\Delta z^+ \sim \mathcal{O}(10)$ (Moser et al., 1999; Lee and Moser, 2015). This means that DNS of flow over riblet-lined walls is approximately 10 times more computationally expensive DNS than for smooth walls, which are already prohibitively expensive at high Reynolds numbers. The stringent resolution requirements make the numerical exploration of riblet-lined wall flows a highly resource-intensive endeavor, significantly limiting the range of Reynolds numbers and configurations that can be practically investigated. Experimental study of riblets poses its own challenges in measurement and manufacturing (Bechert and Bartenwerfer, 1989; Bechert et al., 2000). For example, there are limited means of obtaining measurements of the flow fields between objects on the order of millimeters and the precision manufacturing of a large number of riblet sizes and configurations is also difficult and time consuming.

The challenges of fully resolved simulations and experimental studies of flow over riblets have motivated the development of reduced-order and low-complexity approaches. One approach is to use a minimal channel, which reduces computational costs by limiting the streamwise and spanwise extent of the calculation domain to the minimal set of structures required to sustain turbulence (Jiménez and Moin, 1991). This simplified setting was shown to predict low-order statistics in smooth wall channel flows with small decreases in accuracy observed only in the outer layer (Jiménez and Moin, 1991; Flores and Jiménez, 2010; Hwang, 2013; MacDonald et al., 2017). The minimal channel setting was adapted to rough walls by Chung et al. (2015), and later used for simulating flow over a range of riblet geometries at low to moderate fiction Reynolds numbers (i.e, $Re_\tau = 180, 395$) (Endrikat et al., 2018; Modesti et al., 2018, 2019; Endrikat et al., 2021; Modesti et al., 2021; Wong et al., 2024). These minimal channel simulations of flow over riblets have proven useful in the study of secondary motions and dispersive stresses, as well as in the evaluation of the instabilities that influence the breakdown of the drag reduction regime.

Another method to improving the tractability of the problem is to adapt input–output analysis approaches based on the Navier–Stokes equations linearized about the turbulent mean flow, see e.g. McKeon and Sharma (2010), to the setting of turbulent flow over riblets. Chavarin and Luhar (2020) used such a framework to demonstrate that the response associated with the single resolvent mode representing structures associated with the near-wall cycle predicts slip velocity associated with drag reduction trends. They further showed that the response associated with structures reminiscent of Kelvin-Helmholtz (KH) rollers reporduces the trends of deterioration in drag-reduction observed in DNS of turbulent flow over blade type riblets seen in e.g., García-Mayoral and Jiménez (2011a) and Endrikat et al. (2018). Ran et al. (2021) similarly employed a spatio-temporal response function associated with the linearized Navier–Stokes equations augmented with a turbulent eddy-viscosity to understand the effect of background turbulence on skin-friction drag. Those results, focusing on triangular riblets, further demonstrated the ability of input–output methods to reproduce drag reduction trends.

The present study adopts a restricted nonlinear (RNL) modeling approach that enables both simulation and simplified analysis of flow over riblets (Viggiano et al., 2024). The RNL dynamics are obtained by decomposing the Navier–Stokes equations into a streamwise-averaged component and streamwise-varying perturbations, and then restricting both the nonlinearity in the perturbation equations and the number of streamwise length scales supporting the dynamics (Farrell and Ioannou, 2012; Thomas et al., 2014, 2015; Farrell and Ioannou, 2017). When the streamwise varying scales are limited to those associated with maximum dissipation in the outer layer, the RNL model has been shown to accurately predict both low-order statistics and spectral properties in turbulent channels at low to moderate Reynolds numbers at significantly reduced computation costs versus DNS, see e.g., Bretheim et al. (2015), Gayme and Minnick (2019) and Minnick and Gayme (2019). Use of this streamwise coherent modeling approach is motivated by the observed prevalence and importance of streamwise coherent structures (Kim and Adrian, 1999; Meinhart and Adrian, 1995; Hutchins and Marusic, 2007; Monty et al., 2007; Guala et al., 2006; Marusic, 2001; Smits et al., 2011) in wall-turbulence as well as their role in the energy amplification, see e.g. Jovanović and Bamieh (2005), Farrell and Ioannou (1993), Cossu et al. (2009), del Álamo and Jiménez (2006) and Hwang and Cossu (2010). This emphasis on the cross-stream motions suggests its applicability to the problem of flow over riblets where secondary flows, comprised of cross stream motions, have been associated with both drag-reduction in flow over riblets and its breakdown (Goldstein and Tuan, 1998; Choi et al., 1993; Lee and Lee, 2001; Boomsma and Sotiropoulos, 2016; Raayai-Ardakani and McKinley, 2017).

Results from simulations at $Re_\tau = 395$ demonstrate that both the low-order statistics and the cross-plane structures associated with the secondary flow are indeed well captured by the RNL model. The potential of the current framework for analyzing different mechanisms contributing to riblet-induced friction modifications is demonstrated through comparisons to DNS predictions of the slip velocity and total stresses contributing to the roughness function. An analysis of the KH instabilities associated with the Reynolds stress reveals that the RNL simulations predict the appearance of corresponding structures only in the specific geometries and spacings known to exhibit these instabilities. These results highlight the promise of the RNL setting as a computationally and analytically tractable approach to further understanding drag variations induced by riblet surfaces.

The remainder of the paper is organized as follows. In Section 2 we describe the problem setting and the RNL equations for flow over riblets. The numerical approach and the different riblet geometries to be simulated are detailed in Section 3. In Section 4 we report a short validation of the DNS code that is employed to evaluate the performance of the RNL model. Section 5 compares RNL and DNS predictions of the mean velocity, roughness function and slip velocity. This discussion is followed by an examination of the secondary motions in Section 6. Section 7 focuses on RNL predictions of the stresses, which have been attributed to the breakdown of riblet induced drag reduction. The paper concludes in Section 8.

2. The RNL model for turbulent flow over riblets

Consider a channel flow with respective streamwise, wall-normal, and spanwise spatial coordinates (x, y, z) and temporal coordinate t. The RNL dynamics are derived from the Navier–Stokes equation, by first decomposing the flow field $\mathbf{u}(x, y, z, t)$ into a streamwise-averaged mean component $\langle \mathbf{u} \rangle_x(y, z, t)$, and streamwise varying perturbations about that mean, $\mathbf{u}_p(x, y, z, t) = \mathbf{u}(x, y, z, t) - \langle \mathbf{u} \rangle_x(y, z, t)$. Here $\langle \cdot \rangle_x = \frac{1}{L_x} \int_0^{L_x} (\cdot)\, \mathrm{d}x$ indicates streamwise-averaging over the streamwise extent L_x. In a Fourier space representation, the streamwise-averaged mean, $\langle \mathbf{u} \rangle_x(y, z, t)$, corresponds to the zero streamwise wavenumber, i.e., $k_x = 0$, where $k_x = 2\pi n / L_x$ is the dimensional streamwise wavenumber for non-negative integer n. The perturbation component, $\mathbf{u}_p(x, y, z, t)$, corresponds to the flow field associated with all of the streamwise varying wavenumbers (i.e., $k_x \neq 0$) supported by the dynamics. The pressure field can similarly be decomposed as $p(x, y, z, t) = \langle p \rangle_x(y, z, t) + p_p(x, y, z, t)$. The RNL equations are then formed by neglecting nonlinear interactions between perturbations that do not contribute to the mean. The resulting RNL evolution equations for flow over riblet-lined walls are

$$\frac{\partial \langle \mathbf{u} \rangle_x}{\partial t} + \langle \mathbf{u} \rangle_x \cdot \nabla \langle \mathbf{u} \rangle_x + \left\langle \mathbf{u}_p \cdot \nabla \mathbf{u}_p \right\rangle_x + \frac{1}{\rho} \nabla \langle p \rangle_x - \nu \nabla^2 \langle \mathbf{u} \rangle_x = \langle \mathbf{f} \rangle_x, \tag{1a}$$

$$\frac{\partial \mathbf{u}_p}{\partial t} + \langle \mathbf{u} \rangle_x \cdot \nabla \mathbf{u}_p + \mathbf{u}_p \cdot \nabla \langle \mathbf{u} \rangle_x + \frac{1}{\rho} \nabla p_p - \nu \nabla^2 \mathbf{u}_p = \mathbf{f}_p, \tag{1b}$$

$$\nabla \cdot \langle \mathbf{u} \rangle_x = \nabla \cdot \mathbf{u}_p = 0, \tag{1c}$$

where the immersed boundary force, $\mathbf{f}(x,y,z,t) = \langle \mathbf{f} \rangle_x(y,z,t) + \mathbf{f}_p(x,y,z,t)$, is used to impose boundary conditions associated with the riblets, ρ is the fluid density, and ν is its kinematic viscosity. Here, ∇ and ∇^2 respectively denote the gradient and the Laplacian operators.

In the RNL framework, the nonlinear interactions terms $\langle \mathbf{u}_p \cdot \nabla \mathbf{u}_p \rangle_x - \mathbf{u}_p \cdot \nabla \mathbf{u}_p$ are systematically neglected, yielding simplified dynamics that can be supported by a small number of streamwise varying modes (Thomas et al., 2015; Farrell et al., 2016). The lower number of streamwise modes and reduced nonlinear interactions between these modes reduces the computational requirements in a Fourier representation, see Bretheim et al. (2018) for further details. The RNL system can self-sustain with different sets of streamwise wavenumbers supporting the dynamics, but the properties of this set affect the statistical properties of the RNL flow field (Bretheim et al., 2015). The streamwise wavenumber support that accurately predicts the low-order statistics at low to moderate Reynolds numbers (i.e., $Re_\tau = 110 - 340$ in Bretheim et al. (2015)) was shown to coincide with the outer-layer peak of the dissipation spectra (Minnick and Gayme, 2019). The structures associated with this wavenumber range have streamwise wavelengths that asymptotically approach a constant value for $Re_\tau \leq 2000$, as discussed in detail in Gayme and Minnick (2019). The model parametrization (i.e., streamwise wavenumber support) that produces the desired statistical features for the Reynolds number considered in this work ($Re_\tau = 395$) is known and specified in the simulation set-up. While this parametrization was developed for flow over smooth walls, the widely accepted concept of outer-layer similarity (Townsend, 1980; Schultz and Flack, 2005; Flack et al., 2007) suggests the same parametrization is applicable to flows over riblets.

3. Numerical approach

We now describe the numerical approach used throughout this work. All simulations employ the DNS mode of the open-source pseudo-spectral code JHU-LESGO (2019), which was previously modified to simulate the RNL equations, see e.g., Bretheim et al. (2015) and Minnick and Gayme (2019). This code employs spectral derivatives in the streamwise and spanwise directions with the 3/2 rule for dealiasing. A centered second-order finite difference scheme with a hyperbolic-tangent stretched coordinate system (Jelly et al., 2014; Wang et al., 2019) is used for the wall-normal direction. The second-order Adams–Bashforth method is used for time marching. This code has been extensively used and validated for large eddy simulations (LES) of wall-bounded turbulent flows over a range of configurations such as urban canopies (Cheng and Porté-Agel, 2015; Giometto et al., 2016), vegetative canopies (Chester et al., 2007; Bai et al., 2012), and complex natural terrains (Anderson et al., 2012; Yang and Meneveau, 2016). The DNS mode of the code has been less utilized, so we provide validation cases for turbulent flow over both smooth walls and riblets in Section 4.

All simulations are carried out in a half-channel configuration unless noted otherwise and employ periodic boundary conditions in the horizontal (i.e., streamwise and spanwise) directions. For the wall-normal direction, stress-free ($\partial u/\partial y = \partial w/\partial y = 0$) and zero permeability ($v = 0$) boundary conditions are imposed at the top of the calculation domain. For the bottom wall, no-slip ($u = w = 0$) and zero permeability ($v = 0$) boundary conditions are employed. The geometries of riblets are imposed via the immersed boundary method (Peskin, 2002). The immersed boundary force in Eq. (1) is defined as (Chester et al., 2007; Fang and Porté-Agel, 2016; Li et al., 2016),

$$\mathbf{f}(x,y,z,t)\Big|_{t=n} = \begin{cases} 0 & \text{when } \varphi > 0 \\ \dfrac{3}{2}\dfrac{1}{\rho}\nabla p\Big|_{t=n} - \dfrac{\mathbf{u}^*}{\Delta t} & \text{when } \varphi \leq 0 \end{cases}, \tag{2}$$

where a signed distance function φ is used to indicate the grid points within the solid ($\varphi \leq 0$) and the fluid ($\varphi > 0$). Here, n indicates the time-step, Δt is the duration of the time-step, and $\mathbf{u}^* = \mathbf{u}|_{t=n} + \Delta t \left(\frac{3}{2}\mathbf{r}|_{t=n} - \frac{1}{2}\mathbf{r}|_{t=n-1} + \frac{1}{2}\nabla p|_{t=n-1} \right)$ is an intermediate velocity, with $\mathbf{r} = -\mathbf{u} \cdot \nabla \mathbf{u} + \nu \nabla^2 \mathbf{u}$ representing the sum of advective and diffusive terms. As described in Eq. (1) this force is decomposed as $\mathbf{f} = \langle \mathbf{f} \rangle_x + \mathbf{f}_p$ in the RNL simulations.

The dynamical restriction of the RNL system reduces its streamwise wavenumber support to a small number of k_x Fourier modes. We exploit this order reduction to reduce computational time by simulating the system without a physical streamwise grid. More specifically, Eqs. (1a) and (1b) are solved in (k_x, y, z, t) space, where the truncated nonlinearity is computed as a convolution. This approach eliminates the need for streamwise transforms to physical space to compute the nonlinearity as a product. Further details regarding the computational approach for RNL simulations using the JHU-LESGO code are provided in Bretheim et al. (2018). In this study, the non-zero streamwise wavenumbers retained in the RNL dynamics (Eq. (1)) are $k_x\delta = 15.5,\ 16,\ 16.5$, where δ is the channel half-height for the smooth wall. These streamwise wavenumbers coincide with the peak of the outer-layer surrogate dissipation spectra (Gayme and Minnick, 2019). Consistent with the notion of outer-layer similarity (Townsend, 1980; Schultz and Flack, 2005), this peak region was found to remain largely unaltered for flows over riblets.

3.1. Case descriptions

All of simulations (except the three DNS validation cases) are performed in the half-channel flow configuration shown in Fig. 1 with a wall-normal extent of $L_y/\delta = 1$. For the smooth wall cases, the friction Reynolds number is set to $Re_\tau = 395$, defined as $\mathrm{Re}_\tau = \delta^+ = u_\tau \delta/\nu$, where ν is the fluid viscosity, and $u_\tau \equiv \sqrt{\tau_w/\rho}$ is the friction velocity. Here, τ_w denotes the wall shear stress and ρ is the fluid density.

We consider the four riblet geometries described in Table 1, which were selected to match the configurations studied in Modesti et al. (2021) and Endrikat et al. (2021). We include a schematic of the simulation setup for flow over symmetric triangular riblets to introduce the parameters of the simulation. Here we include the protrusion height, ℓ_T, which is induced through the riblet geometry and necessitates the definition of both a simulation Reynolds number, δ_R^+, taken from the mean height of the riblet, y_m, and a Reynolds number, $\delta_R'^+$, based on the virtual origin for the flow field, ℓ_T below the riblet tip. The latter needs to be considered in comparing flows over rough and smooth walls. More details on the calculation of the virtual origin and the use of the two Reynolds numbers are given in Sections 5 and 6, respectively.

For each geometry we consider spacings of $s^+ = \{10, 15, 20, 25, 30, 40, 50\}$. The riblet heights change with s^+ according to their shape constraints, i.e., $h = s\tan(\pi/2 - \alpha/2)/2$ for symmetric triangular riblets (with a ridge angle $\alpha = \pi/3$), and $h = s/2$ for all the other geometries. The specification of the blade geometry also includes a thickness-to-spacing ratio $b/s = 1/5$. The full details of the geometry for all cases are provided in Table 1.

The details of the computational grid and simulation domain for riblet configurations of the DNS and RNL simulations are provided in Table 2. A spanwise resolution of $\Delta z^+ = 1$ was selected based on previous results that demonstrated that this resolution was adequate to resolve both the riblet geometry and the smallest turbulent scales (Goldstein and Tuan, 1998; García-Mayoral and Jiménez, 2011b).

4. DNS code validation

We next validate the DNS mode of the JHU-LESGO code for full channel flow with smooth walls at $Re_\tau = 180$ and 395, and a channel with a smooth top wall and riblets over the bottom wall at $Re_\tau = 180$. For the smooth wall configuration we impose no-slip boundary conditions at both the top and bottom wall. For the simulation at $Re_\tau = 180$, we employ a domain size of $[L_x, L_y, L_z]/\delta = [4\pi, 2, 4\pi/3]$ with $[N_x, N_y, N_z] = [128, 192, 128]$ grid points, corresponding to grid

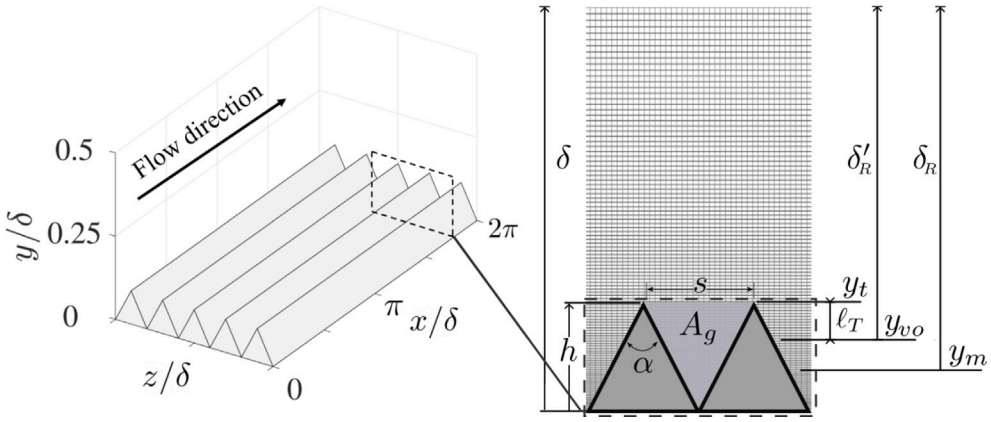

Fig. 1. Schematic diagram of the flow configuration with symmetric triangular riblets as an example (not to scale). Included is the height of the riblet, h, the spacing, s, the angle of the riblet tip, α, the area of the cross-section, A_g, and the half-channel height from the base, i.e. the smooth wall half-channel height, δ. Also presented is the mean height of the riblets, y_m, and the associated half-channel height of the riblets δ_R. We introduce the virtual origin, y_{vo}, in the wall-normal direction which is located ℓ_T below the riblet tip, y_t, where ℓ_T is the protrusion height and the adjusted channel height, δ_R' is taken from the virtual origin.

Table 1
Description of the riblet geometries considered. Cases are denoted by XX##, where (XX) indicates the geometry and (##) indicates spacing s^+. We use 'ST' for symmetric triangular, 'BL' for blade, 'AT' for asymmetric triangular, and 'TR' for trapezoid geometries. The area of the cross section between the riblets elements is denoted A_g^+, which is used to define the characteristic length $\ell_g^+ = \sqrt{A_g^+}$. Finally, the half-channel height measured from the virtual origin, $\delta_R'^+$, is included.

Geometry	Case	s^+	h^+	ℓ_g^+	α	b/s	$\delta_R'^+$
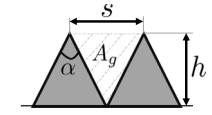 Symmetric triangular	ST10	10	8.66	6.58	$\pi/3$	–	379.2
	ST15	15	12.99	9.87	$\pi/3$	–	373.1
	ST20	20	17.32	13.16	$\pi/3$	–	366.3
	ST25	25	21.65	16.45	$\pi/3$	–	359.7
	ST30	30	25.98	19.74	$\pi/3$	–	353.2
	ST40	40	34.64	26.32	$\pi/3$	–	340.4
	ST50	50	43.30	32.90	$\pi/3$	–	327.9
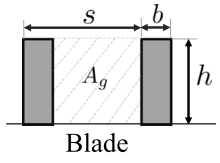 Blade	BL10	10	5	6.32	–	1/5	388.0
	BL15	15	7.5	9.47	–	1/5	385.6
	BL20	20	10	12.65	–	1/5	383.1
	BL25	25	12.5	15.81	–	1/5	380.6
	BL30	30	15	18.97	–	1/5	378.1
	BL40	40	20	25.30	–	1/5	373.1
	BL50	50	25	31.62	–	1/5	368.1
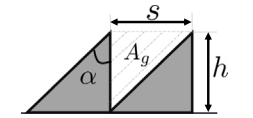 Asymmetric triangular	AT10	10	5	5	0.35π	–	385.3
	AT15	15	7.5	7.5	0.35π	–	381.9
	AT20	20	10	10	0.35π	–	378.0
	AT25	25	12.5	12.5	0.35π	–	374.6
	AT30	30	15	15	0.35π	–	370.9
	AT40	40	20	20	0.35π	–	363.6
	AT50	50	25	25	0.35π	–	356.4
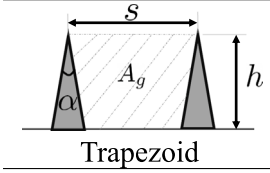 Trapezoid	TR10	10	5	6.58	$\pi/6$	–	387.5
	TR15	15	7.5	9.87	$\pi/6$	–	385.2
	TR20	20	10	13.16	$\pi/6$	–	382.6
	TR25	25	12.5	16.45	$\pi/6$	–	379.9
	TR30	30	15	19.74	$\pi/6$	–	377.3
	TR40	40	20	26.32	$\pi/6$	–	372.0
	TR50	50	35	32.90	$\pi/6$	–	366.7

Table 2
Description of the computational domain and grid resolution for the DNS and RNL simulations. L_x, L_y and L_z are the streamwise, wall-normal and spanwise extents, while N_x, N_y and N_z are the corresponding number of grid points, Δx^+, Δy^+ and Δz^+ are the corresponding grid resolutions.

Case	L_x/δ	L_y/δ	L_z/δ	N_x	N_y	N_z	Δx^+	Δy^+	Δz^+
DNS	2π	1	3.0380	288	192	1200	8.6176	0.6205~3.4092	1
RNL	–	1	3.0380	–	192	1200	–	0.6205~3.4092	1

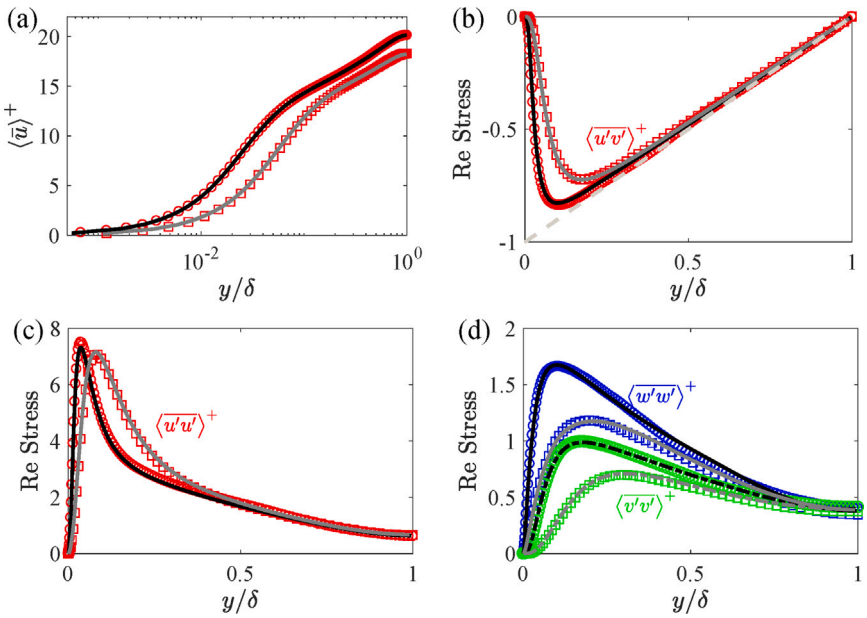

Fig. 2. Validation of JHU-LESGO DNS code for smooth wall channel flow at $Re_\tau = 180$ and 395. Panel (a) shows the time- and plane-averaged streamwise velocity, $\langle\overline{u}\rangle^+$, and panels (b-d) show Reynolds stresses. The black ($Re_\tau = 180$) and gray ($Re_\tau = 395$) lines indicate the results from the JHU-LESGO code. Markers indicate data from Moser et al. (1999) at $Re_\tau = 180$ (○) and $Re_\tau = 395$ (□).

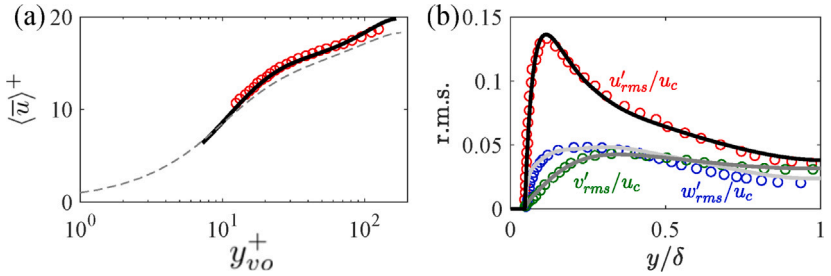

Fig. 3. Validation of JHU-LESGO DNS code for riblet-lined wall channel flow at $Re_\tau = 180$. Panel (a) shows the time- and plane-averaged streamwise velocity, $\langle\overline{u}\rangle^+$, and (b) depicts the root mean square (r.m.s.) of velocity fluctuations, normalized by the mean channel centerline velocity $u_c = \langle\overline{u}(y=\delta)\rangle$. The lines indicate the results from the JHU-LESGO code. Circle markers (○) represent data from Choi et al. (1993). In panel (a), y^+_{vo} denotes the wall-normal coordinate starting from the virtual origin, chosen using the method of Bechert and Bartenwerfer (1989) to match the profile with cross markers (+) data in Fig. 8 of Choi et al. (1993). The dashed gray line represents the smooth wall results from Moser et al. (1999) for reference.

resolutions of $\Delta x^+ \approx 17.7$, $\Delta y^+ \in [0.2, 3.5]$, and $\Delta z^+ \approx 5.9$. For the $Re_\tau = 395$ case, the domain size is $[L_x, L_y, L_z]/\delta = [2\pi, 2, \pi]$ with $[N_x, N_y, N_z] = [256, 384, 192]$ grid points, corresponding to grid resolutions of $[\Delta x^+, \Delta y^+, \Delta z^+] \approx [9.7, 0.1 \sim 1.7, 6.5]$. These resolutions were chosen to match those of Moser et al. (1999) in the streamwise and spanwise directions. The finest resolution in the wall-normal grid was also selected to be similar to that of Moser et al. (1999), however, the range differs due to our use of a hyperbolic-tangent stretched coordinate system rather than the Chebyshev grid employed in Moser et al. (1999).

Fig. 2(a) shows the time- and plane-averaged streamwise velocity, $\langle\overline{u}\rangle^+$, for the two smooth wall cases. Here the angle brackets indicate plane-averaging, i.e., $\langle\cdot\rangle = \frac{1}{L_x}\frac{1}{L_z}\int_0^{L_z}\int_0^{L_x}(\cdot)\,\mathrm{d}z\,\mathrm{d}x$, the over-bar indicates time-averaging, $\overline{\cdot} = \frac{1}{T}\int_0^T(\cdot)\,\mathrm{d}t$, and the + subscript indicates wall-units, i.e., $u^+ = u/u_\tau$. Reynolds stresses are shown in Fig. 2(b)–(d), where $(\cdot)' = (\cdot) - (\overline{\cdot})$ is the fluctuation. These results demonstrate that the DNS mode of the JHU-LESGO code accurately reproduces both the first- and second-order statistics reported in Moser et al. (1999) at both Reynolds numbers.

We validate this code for flow over riblets using the full channel flow configuration in Choi et al. (1993), where the upper wall is smooth and the lower wall geometry comprises symmetric triangular riblets with a ridge angle of $\alpha = \pi/3$, and riblet spacings of $s^+ = su_\tau/\nu = 20$. We perform the simulation at $Re_\tau = 180$ with the same domain size as Choi et al. (1993), which is $[L_x, L_y, L_z]/\delta = [\pi, 2, 0.289\pi]$, with $[N_x, N_y, N_z] = [32, 192, 160]$ grid points corresponding to a grid resolution of $[\Delta x^+, \Delta y^+, \Delta z^+] \approx [17.7, 0.2 \sim 3.5, 1]$. For a direct comparison of the results, we map our vertical direction coordinate frame to that used in Choi et al. (1993).

Fig. 3 shows that both the mean streamwise velocity and the root mean square (r.m.s.) statistics of each velocity components, respectively in panels (a) and (b), compare well with those of Choi et al. (1993). In particular, the upward shift in the mean streamwise velocity compared to the smooth wall profile (shown as a dashed line in Fig. 3(a)) is well captured, indicating our ability to predict the drag reduction induced for this riblet geometry.

The next three sections discuss RNL predictions of key flow properties and associated analysis for the geometries described in Table 1.

5. Mean momentum transfer analysis

In this section, we evaluate the ability of the RNL model to predict riblet induced alterations to skin friction drag and the corresponding slip velocity for the various riblet geometries in Table 1. We quantify changes in skin friction drag using the roughness function, ΔU^+, defined in terms of the upward/downward shift in the logarithmic profile

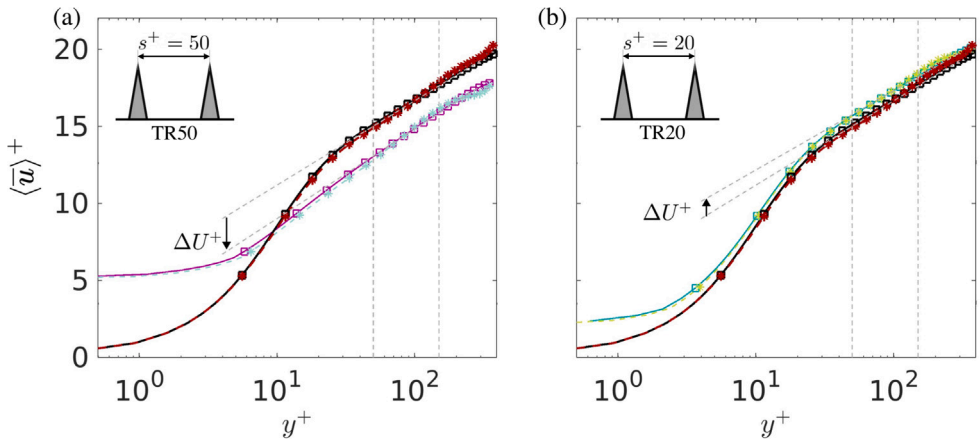

Fig. 4. Time- and plane-averaged streamwise velocity $\langle \overline{u} \rangle^+$ from DNS (square □ markers) and RNL (∗ markers). (a) smooth wall DNS (□) and RNL simulation (∗) streamwise velocity predictions compared to profiles from drag increasing case TR50 from DNS (□) and RNL simulations (∗). (b) smooth wall DNS (□) and RNL simulation (∗) compared to profiles from drag decreasing case TR20 from DNS (□) and RNL model (∗). In both panels, vertical dashed lines indicate the position of $y^+ = 50$ and 150 as references, and the slanted dashed lines are used to evaluate the roughness function ΔU^+.

due to the addition of riblets (Flack and Schultz, 2010),

$$\langle \overline{u} \rangle^+ = \frac{1}{\kappa} \ln \left[y^+_{v0} \right] + B - \Delta U^+. \tag{3}$$

Here $\kappa = 0.4$ is the Von Kármán constant, $B = 5.2$ is a constant representing the wall-normal intercept of the logarithmic profile for the smooth wall case (Pope, 2001), and y^+_{vo} is the virtual origin of turbulence (Luchini et al., 1991). We follow the method of Endrikat et al. (2021) and define $y^+_{vo} = (y + h - \ell_T)^+$ where ℓ_T is the protrusion height (Luchini et al., 1991), and h is the riblet height (see Table 1). We determine ℓ^+_T based on the largest slope of the Reynolds stress profile at the drag optimum case for each riblet type. This ℓ^+_T/h^+ is then used for all riblet spacings. For ease of exposition we redefine our current coordinate system and use $y^+ = 0$ at the virtual origin for all subsequent rough-wall representations and calculations.

Fig. 4(a) shows the time- and plane-averaged streamwise velocity, $\langle \overline{u} \rangle^+$, as a function of the wall-normal elevation y^+ for DNS and RNL simulations of flow over riblets with a spacing associated with drag increase (case TR50). Here, the RNL simulation accurately predicts the mean velocity profile for the smooth wall and the velocity reduction induced by the drag-increasing riblet configuration. Fig. 4(b) provides the streamwise velocity for the flow over riblets with a spacing associated with drag reduction (case TR20). As in panel (a), the RNL simulation accurately reproduces the rough-wall mean velocity profiles and the drag reduction associated with this case. Similar accuracy in the mean velocity profile is seen across the range of cases in Table 1. The accuracy of the RNL model in predicting the mean velocity profile and roughness function across these cases, using the same wavenumbers effective for smooth wall flows, stems from outer-layer similarity. While riblets may alter near-wall structures, the turbulent cascade in the outer layer remains unaffected, with dissipative streamwise scales unaltered.

Fig. 5 shows DNS and RNL predictions of the roughness function ΔU^+ as a function of the characteristic length-scale ℓ^+_g alongside results from the minimal channel DNS of Endrikat et al. (2021). Here we compute ΔU^+ based on the differences of linear fits to the smooth- and rough-wall velocity profiles over the range $y^+ \in [50, 150]$. Our DNS results are comparable to the minimal channel results of Endrikat et al. (2021), but with small differences in the precise ΔU^+ values. These differences may be associated with the difference in the roughness function measurement approach, i.e., the fact that the roughness function can be evaluated at any location in the logarithmic range, which is known to lead to small differences in the precise values but not the overall trends. Additional differences may be attributed to the full versus minimal channel simulation domains, the half-channel versus full-channel settings, and the differences in Reynolds number due to the change in the channel height because of the riblets lining the lower wall. The figures indicate that the RNL model accurately predicts the point of maximum drag reduction as $\ell^+_{g-opt} \approx 10$ for all of the geometries considered in this study. These results are consistent with the reference data of Endrikat et al. (2021) for the same geometries in a minimal channel configuration. For example, the blade case of the RNL simulations predict $\ell^+_{g-opt} \approx 9.87$, which is the closest spacing to the value predicted in DNS by García-Mayoral and Jiménez (2011b), who reported $\ell^+_{g-opt} \approx 10.7$. Our value is also in close agreement with experimental results from Bechert et al. (1997), who found $s^+_{opt} \approx 18$ (which corresponds to $\ell^+_{g-opt} \approx 10$). Analysis based on an eddy-viscosity enhanced linearized Navier–Stokes equations based models predict similar trends and the correct minimal drag spacing for trapezoidal riblets with the same $\alpha = 60°$ at $Re_\tau = 186$ (Ran et al., 2021) but slightly overestimate the drag reduction. Our results have closer correspondence to the DNS, which suggests that essential physics governing drag reduction and its subsequent breakdown are effectively captured by the RNL model.

We further examine the mean flow characteristics using the slip velocity, which is defined as the time- and plane-averaged streamwise velocity at the riblet tip. The slip velocity for all considered RNL and DNS cases is presented in Fig. 6. These figures show that the slip velocity magnitude increases nearly linearly with the characteristic riblet length scale up to a certain value and then becomes sublinear. Taking the blade geometry as an example (Fig. 6(a)), the slip velocity increases linearly with increasing riblet length scale in the viscous regime (i.e., $0 \leq \ell^+_g \leq 10$), and the slope of the line follows the Stokes flow based predictions proposed by Luchini et al. (1991), i.e., the dashed gray line in Fig. 6(a). When the riblets length scale is larger, i.e., $\ell^+_g \geq 15$, the DNS results deviate from the Stokes prediction. This is expected since the riblets are above the viscous sublayer, where the linear assumption of Stokes flow is no longer applicable. Previous studies using a low-order resolvent analysis based model demonstrated similar agreement in the magnitude trend within the regime where the Stokes flow assumption is valid (Chavarin and Luhar, 2020), but begins to deviate at larger spacings. Further analysis, beyond the scope of the current study, is needed to assess whether this breakdown is due to the limited number of resolvent modes used in their analysis or can be attributed to the linearity of the resolvent model. The RNL captures the magnitude trend and accurately predicts the deviation from the Stokes behavior (seen most clearly in Fig. 6(a)) for all geometries. These results indicate that the nonlinearity maintained in the RNL model is sufficient to capture the behavior associated with the known deviations of the slip velocity at large spacing, which suggests the potential of

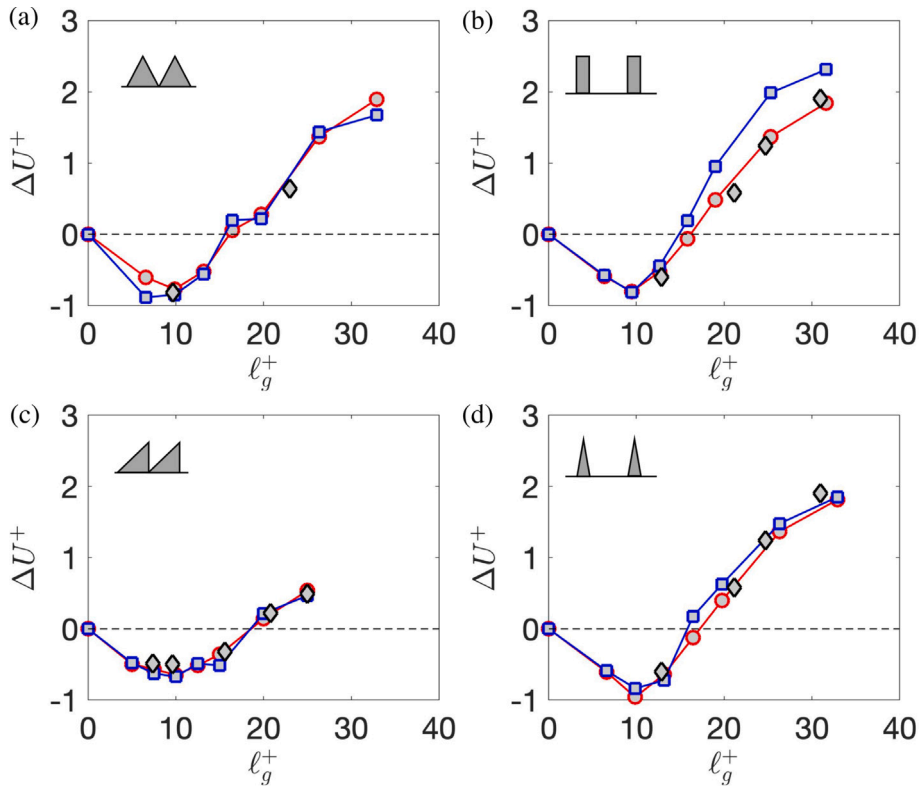

Fig. 5. Roughness function, ΔU^+, as a function of the equivalent riblet length ℓ_g^+ for (a) symmetric triangular, (b) blade, (c) asymmetric triangular, and (d) trapezoid riblets as reported from DNS (○), RNL simulations (□), and minimal channel simulations (◇) from Endrikat et al. (2021).

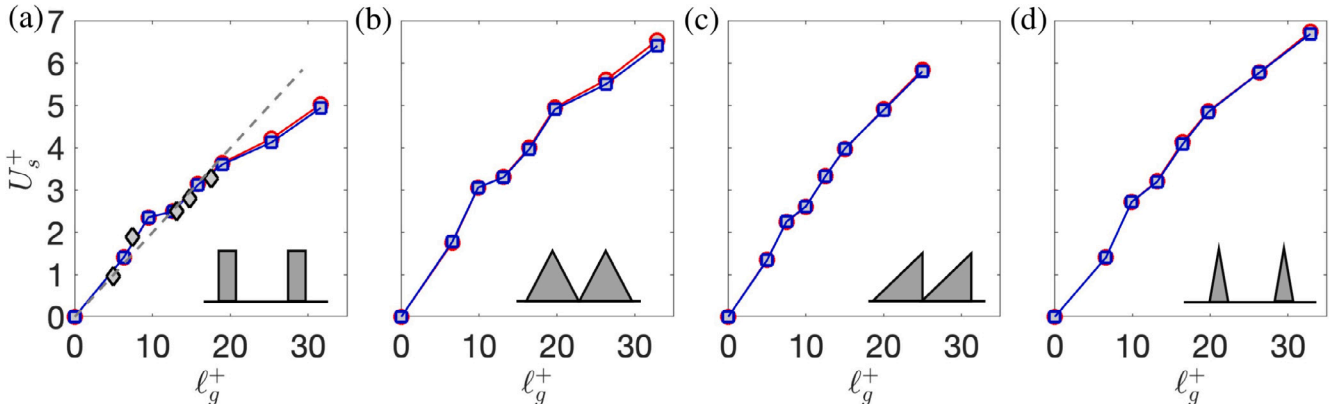

Fig. 6. Slip velocity, U_s^+, as a function of ℓ_g^+ for different geometries. In all panels, ○ indicates DNS results, and □ RNL model predictions. In panel (a), DNS results from García-Mayoral and Jiménez (2011b), represented with ◇, and Stokes predictions (Luchini et al., 1991), represented with – –, are also included for reference.

this model in studying the regime where riblet induced drag reduction breaks down.

Figs. 4–6 demonstrate the accuracy of the RNL predictions of the spacing associated with the minimal drag, the overall roughness function and slip velocity trends across a wide range of riblet geometries and sizes. We next examine its ability to reproduce the cross-plane motion and associated secondary flow structures.

6. Secondary flow structures induced by riblets

The secondary flow motions result in non-zero mean cross-plane velocities in the immediate vicinity of the riblet geometry. We examine this behavior in terms of the time- and streamwise-averaged wall-normal velocity, $\langle \bar{v} \rangle_x^+$, in Fig. 7. The figure presents data obtained from both DNS and RNL simulations for different riblet geometries at four spacings. In particular, panels (a) and (b) show symmetric triangular, (c) and (d) asymmetric triangular, (e) and (f) blade, and, (g) and (h) trapezoid shaped riblets. In each panel, the first two columns are in the drag reducing regime with the second column corresponding to the optimal spacing or minimal drag configuration for the particular geometry. The data in the third column corresponds to the spacing at which the riblets cross over from reducing to increasing drag, we refer to this spacing as the neutral point as the smooth- and rough-wall friction drag are approximately equal for this spacing. The fourth column corresponds to a spacing in the increased friction drag regime. The vertical dashed lines are included to separate the drag reduction, neutral, and increased drag cases.

For the symmetric configurations (i.e., blade, symmetric triangular, and trapezoid shapes), the velocity moves upward above the riblet tip (illustrated by red contours), and downward into the valley (shown

via blue contours). This pattern of alternating high and low vertical velocity near the riblets is a form of Prandtl's secondary flow (Prandtl, 1931). For the asymmetric triangular case, positive vertical velocity is present in the valley as well as above the riblet tip, while downward movement is observed at the middle of the hypotenuse of the triangle. This behavior is consistent with observations of Modesti et al. (2018). Comparisons of the DNS and RNL simulation results for each geometry considered here indicate that both the location and the intensity of vertical motions with increasing spacing that has been associated with increasing modification to the near-wall turbulent structures (Chung et al., 2018) are well represented by the RNL model.

Fig. 8 plots the mean streamwise vorticity, $\overline{\omega}_x = \partial\bar{w}/\partial y - \partial\bar{v}/\partial z$ obtained from DNS and RNL simulations for all of the geometries and spacings in Fig. 7. In all RNL and DNS cases, there are two regions with an alternating pattern of high and low mean streamwise vorticity. In particular, small high and low vorticity regions in the immediate vicinity of the riblet surface are accompanied by larger regions of vorticity with the opposite sign directly above them. This vorticity is confined to a wall-normal distance that is less than two times the riblet spacing. Although there are some similarities in the structures for all cases, the different geometries lead to slightly different arrangements and positioning of the regions with alternating sign vorticity. For the symmetric configurations (i.e., blade, symmetric triangular, and trapezoid), the large-regions of alternating signed streamwise vorticity extends farther into the riblet valley, enhancing momentum flux in the valley region. These results indicate that the RNL simulations are able to reproduce the size and intensity of vorticity in the cross-plane as well as the variation as a function of increasing spacing for all of the geometries in Table 1.

The high accuracy of the RNL predictions for secondary motions is not unexpected, since the cross-plane scales are fully resolved and the streamwise mean nonlinearity is retained in the RNL dynamics. This nonlinearity has been previously shown to be responsible for re-distributing momentum and generating instantaneous streamwise rolls, see e.g. Reddy and Ioannou (2000), Gayme et al. (2011) and Gayme and Minnick (2019) and the references therein. In the context of flow over riblets, this nonlinearity also responds to the near-wall topography, intensifying with increasing riblet size, and modifying the near-wall rolls induced by the secondary flow as illustrated in Figs. 7 and 8. We also expect streamwise perturbations that interact to contribute to the mean, i.e., $\langle \mathbf{u}_p \cdot \nabla \mathbf{u}_p \rangle_x$, to play a role in the generation of these streamwise-rolling motions. Furthermore, as the streamwise perturbations scale with the outer-layer surrogate dissipation spectra, we expect them to become more dominant farther from the wall and be relevant when the riblets protrude into the outer-layer. The trends observed indicate that the essential physics governing drag reduction and its subsequent breakdown are effectively captured by the RNL model. In the next section we take steps towards quantifying such effects on drag reduction and its associated breakdown by isolating the effect of stresses in the roughness function.

7. The role of total stresses

We now decompose the roughness function to isolate the total stress component and explore the role of these stresses in riblet-induced friction drag reduction and its breakdown. Following the approach of Endrikat et al. (2021) we start from the momentum balance for flow above a heterogeneous rough surface,

$$\frac{1}{\rho}\frac{\mathrm{d}P}{\mathrm{d}x} = -\frac{1}{\delta}\frac{\tau_w}{\rho} = -\frac{\mathrm{d}\langle\overline{u'v'}\rangle}{\mathrm{d}y} - \frac{\mathrm{d}\langle\overline{\tilde{u}\tilde{v}}\rangle}{\mathrm{d}y} + \nu\frac{\mathrm{d}^2\langle\bar{u}\rangle}{\mathrm{d}y^2}, \tag{4}$$

where $(\tilde{\cdot}) := (\cdot) - \langle\cdot\rangle$ is the horizontal spatial fluctuation and $\langle\overline{\tilde{u}\tilde{v}}\rangle$ represents the dispersive stress. Then we integrate the equation with respect to the wall-normal component, and express the total stress as the sum of Reynolds, dispersive, and viscous stresses. These integrated stress profiles at a given critical channel height (y_c^+ in the logarithmic layer) are given by

$$\langle\bar{u}\rangle^+|_{y=y_c^+} = \int_{y_t^+}^{y_c^+} \frac{\delta_R'^+ - y^+}{\delta_R^+}\mathrm{d}y^+ + \int_{y_t^+}^{y_c^+} \left(\langle\overline{u'v'}\rangle^+ + \langle\overline{\tilde{u}\tilde{v}}\rangle^+\right)\mathrm{d}y^+ + \langle\bar{u}\rangle^+|_{y=y_t^+}. \tag{5}$$

Here, y_t^+ is the location of the riblet tip, $\delta_R^+ = 395 - y_m^+$ represents the Reynolds number taken from the mean height of the riblet, and $\delta_R'^+$ represents the true Reynolds number based on the adjusted origin of turbulence (see Fig. 1 and Table 1). Using a similar approach, the mean streamwise velocity of the smooth wall (denoted by a subscript sw) can be expressed as:

$$\langle\bar{u}_{\mathrm{sw}}\rangle^+|_{y=y_c^+} = \int_{y_t^+}^{y_c^+} \frac{\delta^+ - y^+}{\delta^+}\mathrm{d}y^+ + \int_{y_t^+}^{y_c^+} \langle\overline{u'v'}_{\mathrm{sw}}\rangle^+\mathrm{d}y^+ + \langle\bar{u}_{\mathrm{sw}}\rangle^+|_{y=y_t^+}. \tag{6}$$

Subtracting Eq. (5) from Eq. (6), leads to the following expression for the roughness function ΔU^+

$$\Delta U^+ = \langle\bar{u}_{\mathrm{sw}}\rangle^+|_{y=y_c^+} - \langle\bar{u}\rangle^+|_{y=y_c^+} = \Delta U_t^+ + \Delta U_{uv}^+, \tag{7}$$

where

$$\Delta U_t^+ = \langle\bar{u}_{\mathrm{sw}}\rangle^+|_{y=y_t^+} - \langle\bar{u}\rangle^+|_{y=y_t^+}, \tag{8}$$

which represents the velocity difference at the height of the riblet tip for smooth and riblet-lined wall, and

$$\Delta U_{uv}^+ = \int_{y_t^+}^{y_c^+} \left(\frac{\delta^+ - y^+}{\delta^+} - \frac{\delta_R'^+ - y^+}{\delta_R^+}\right)\mathrm{d}y^+ + \int_{y_t^+}^{y_c^+} \left(\langle\overline{u'v'}_{\mathrm{sw}}\rangle^+ - \langle\overline{u'v'}\rangle^+ - \langle\overline{\tilde{u}\tilde{v}}\rangle^+\right)\mathrm{d}y^+. \tag{9}$$

This ΔU_{uv}^+ is defined as the total stress component, representing the change related to both the dispersive stress components and the difference in Reynolds number due to the change from the smooth versus riblet-lined wall configuration.

Fig. 9 shows the components of the roughness function decomposition in Eq. (7) and their sum alongside the roughness function computed from the velocity curves (previously described in Fig. 5). For the DNS cases, and all but the RNL simulations over blade riblets the total drag reduction curve (dashed black line in Fig. 9) closely matches the curve obtained using Eq. (7) through most of the range of ℓ_g^+. In all cases, the total stress component shows negligible contributions in the drag reduction regime, i.e., the drag reduction is driven by ΔU_t^+ in the viscous regime. ΔU_{uv}^+ begins to contribute to the total drag around $\ell_g^+ \sim 15$ and begins to dominate as the riblet induced drag reduction breaks down and the flow moves into an increased drag regime. For each component, the general trends predicted by the RNL simulations and DNS are consistent. For example, the total stress component (blue square) contributes minimally for the small ℓ_g^+, while an increased effect is observed at a similar threshold as in the DNS. Moreover the ΔU_t^+ values obtained from the RNL simulations are similar to the DNS values across all cases except the symmetric triangular riblet simulations. In fact, the largest discrepancy between DNS and RNL occurs for the smallest riblet spacings for the symmetric triangles (see Fig. 9(b) and (f)). The origin of this difference is unclear and may be due the sensitivity of the computation to the method of obtaining ℓ_T^+. This is also noted in the similar error observed between ΔU^+ computed from Eq. (7) and ΔU^+ calculated from the velocity curves at that spacing. This trend is not observed by neighboring spacings, indicating that this discrepancy does not arise from the RNL physics.

There are also differences between DNS and RNL predictions at the largest spacings for both the blade and triangular riblet cases. For the blade riblet simulations the RNL model slightly over-predicts the stresses in the drag-increasing regime, panels (a) and (e). These differences are also reflected in an over prediction of the roughness function using the decomposition in Eq. (7) for the RNL simulations.

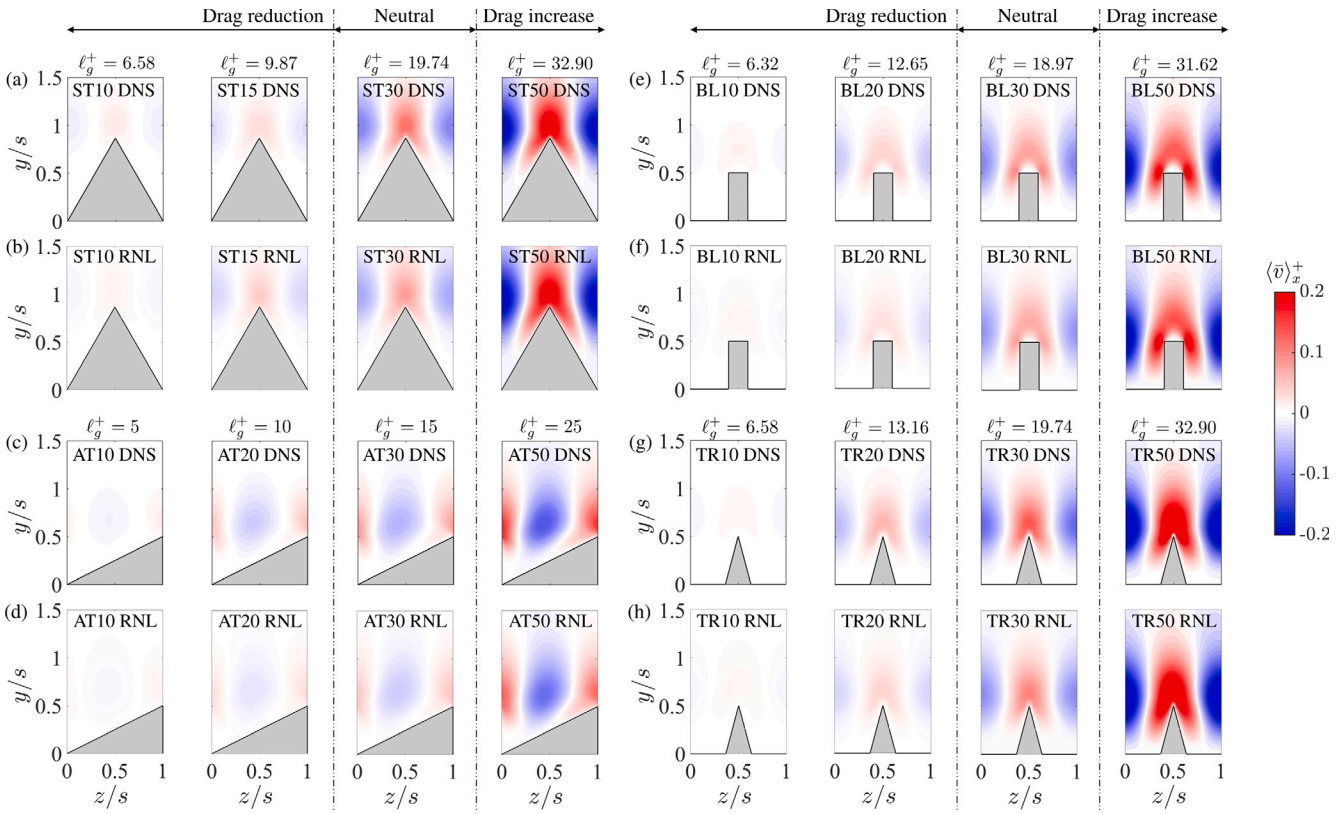

Fig. 7. Time- and streamwise-averaged wall-normal velocity, $\langle \bar{v} \rangle_x^+$, illustrating the secondary flow motions in the cross-plane. In all panels, positive wall-normal velocity (shown in red) corresponds to flow upwards, and negative wall-normal velocity (shown in blue) represents downward flow. For each geometry, the left two columns are in the drag reducing regime and the second column represents the minimum drag point; the third column corresponds to the neutral point; and the fourth column is in drag increasing regime.

The decomposition recovers the measured function, which suggests that there is an effect that is not captured in the RNL simulations over the blades in the drag increasing regime. In contrast, the total stresses are under-predicted for the same spacing regime for the symmetric triangular riblets. However in this case, the corresponding over prediction of ΔU_t^+ leads to a similar overall prediction for the roughness function. Future work is needed to determine the source of these differences, particularly to extract the Reynolds number differences (in the smooth versus rough-wall simulations) and riblet induced physics.

It is of interest to note that the over prediction of the stresses in the drag increasing regime occurs in the blade riblet case, where a KH instability is thought to play a role in the degradation of the drag reduction process (García-Mayoral and Jiménez, 2011b; Endrikat et al., 2021). In order to further explore this connection, we investigate the capability of the RNL model to predict KH-like rollers over riblets by analyzing the premultiplied 2D co-spectra of the Reynolds stress. Fig. 10 provides this quantity at an $x-z$ plane located 3 wall units above the riblet tips for all four riblet types. The three columns respectively show data for RNL cases with spacings, $s^+ = 30$, 40, 50, where the corresponding ℓ_g^+ is noted at the top of each panel alongside a schematic of the riblet geometry. In each panel, the $\lambda_z^+ = s^+$ value is marked with a line and the region pertaining to the scales that are relevant to KH-like rollers ($65 < \lambda_x^+ < 290$ and $250 < \lambda_x^+ < \infty$) is outlined by a solid box. The three non-zero streamwise wavenumbers supporting the RNL dynamics ($k_x\delta = 15.5,\ 16,\ 16.5$) correspond to $\lambda_x \approx 160, 155,$ and 150. These modes are captured in the single elongated structure that spans the simulated wavelengths in the 2D spectra in Fig. 10. Here it is clear that the RNL model accurately predicts the main peak, which is known to be primarily associated with turbulence, and the near-wall streaks indicating the model reproduces non-riblet related flow properties. Moreover, the signature of the texture at $\lambda_z^+ = s^+$ is also well modeled by the limited streamwise wavenumbers in the RNL dynamics for the blade riblets, consistent with previous findings (Viggiano et al., 2024). As noted in Viggiano et al. (2024), the normalized magnitude of the RNL spectra is larger than that of the minimal channel due to the fact that energy is constrained to a small number of modes that must contribute to the same total stress that Fig. 9 indicates is consistent with that observed in the DNS (minimal channel) data that has a full range of streamwise scales.

Fig. 10 shows substantial stresses within the boxed region ($65 < \lambda_x^+ < 290$ and $250 < \lambda_x^+ < \infty$) for all riblets types except the asymmetric triangular riblets. The highest levels of stress are seen in the blade cases. Stress within the boxed region is observed for both the symmetric triangular riblets at $\alpha = 30°$ and the trapezoidal riblets, though it is less pronounced compared to the blade case. This progression aligns with the spectral analysis of Endrikat et al. (2021). In the RNL model, for the three cases in which the KH instability plays a role, it reaches its maximum within the box at $s^+ = 30$ (left-most column of Fig. 10) and then diminishes as s^+ increases. When comparing with the specific wavenumber magnitude observed by Endrikat et al. (2021), a decrease in stress is detected, again matching our trends, but the stresses shift towards larger wavenumbers still associated with KH-like rollers as the spacing increases. Although the RNL model is not able to fully capture this effect, trends in total stress do not clearly suggest that it is a key factor in the differences between the RNL model and DNS curves. Further isolation of the contributions of KH rollers needs to be performed to understand the implications of the limited band of wavenumbers on the generation of the KH instability. These results suggest that overall, the RNL model is able to capture the signature of the KH-like rollers in the drag increasing regime even with the vastly reduced streamwise varying modes supporting the RNL dynamics. Although this may seem surprising, the ability to reproduce these structures is

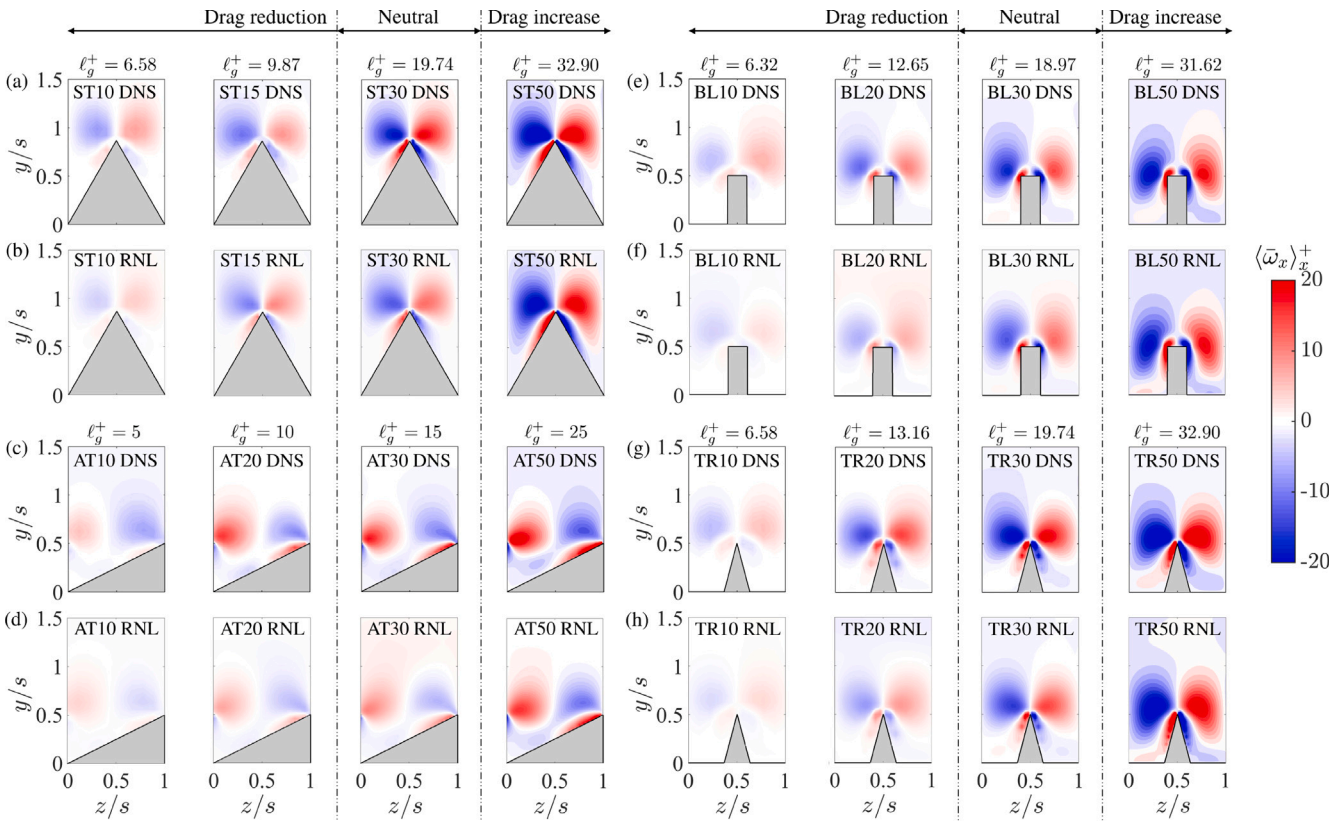

Fig. 8. Time- and streamwise-averaged streamwise vorticity, $\langle \overline{\omega}_x \rangle_x^+$, from DNS and RNL simulations for each geometry. In all panels, positive vorticity (shown in red) corresponds to clockwise-rotating fluid, and negative vorticity (shown in blue) represents counterclockwise-rotating fluid. For each geometry, the left two columns are in the drag reducing regime and the second column represents the minimum drag point; the third column corresponds to the neutral point; and the fourth column is in drag increasing regime.

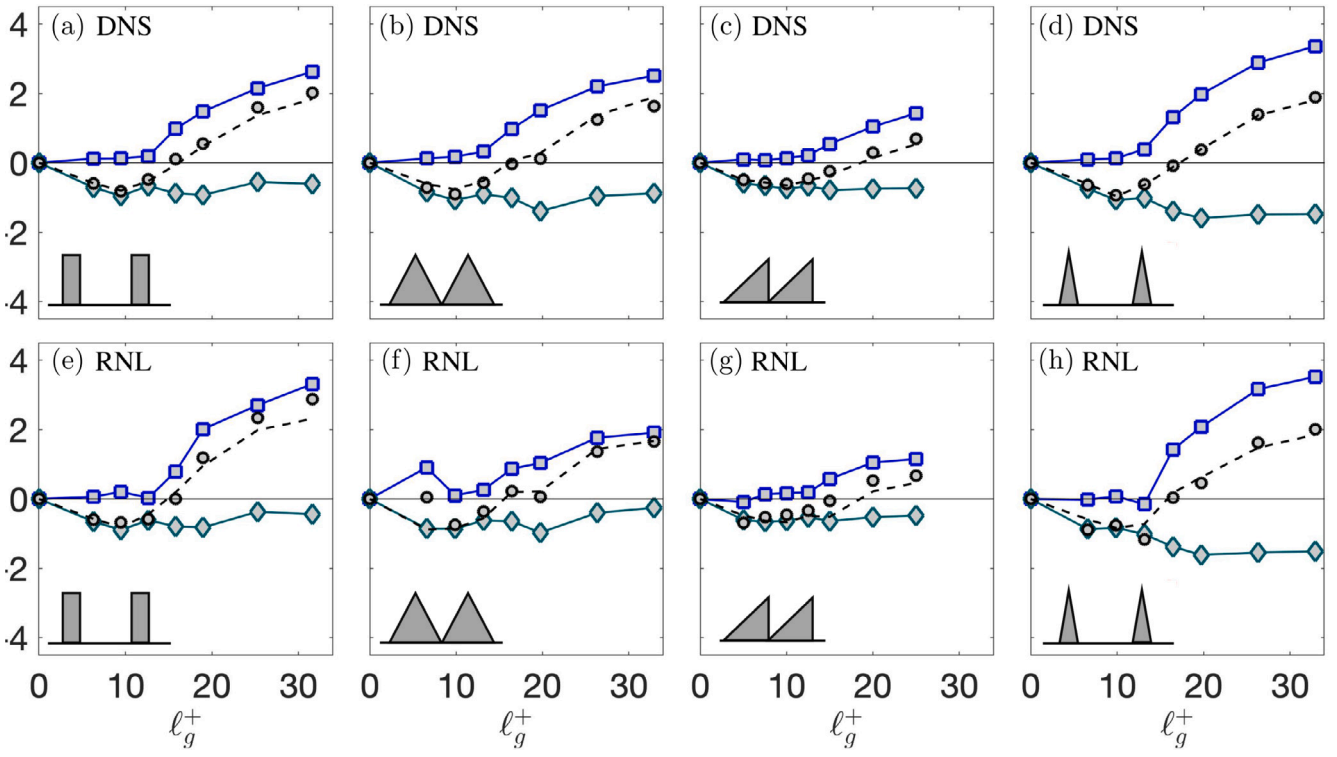

Fig. 9. Roughness function components from Eq. (7) as a function of ℓ_g^+ for different geometries obtained from DNS (top panels) and RNS simulations (bottom panels). All panels show the total stress, ΔU_{uv}^+ (□), ΔU_t^+ (◇), and the addition of these two terms (○), for comparison with the total drag reduction (––) based on the velocity profile shift (reproduced from Fig. 5).

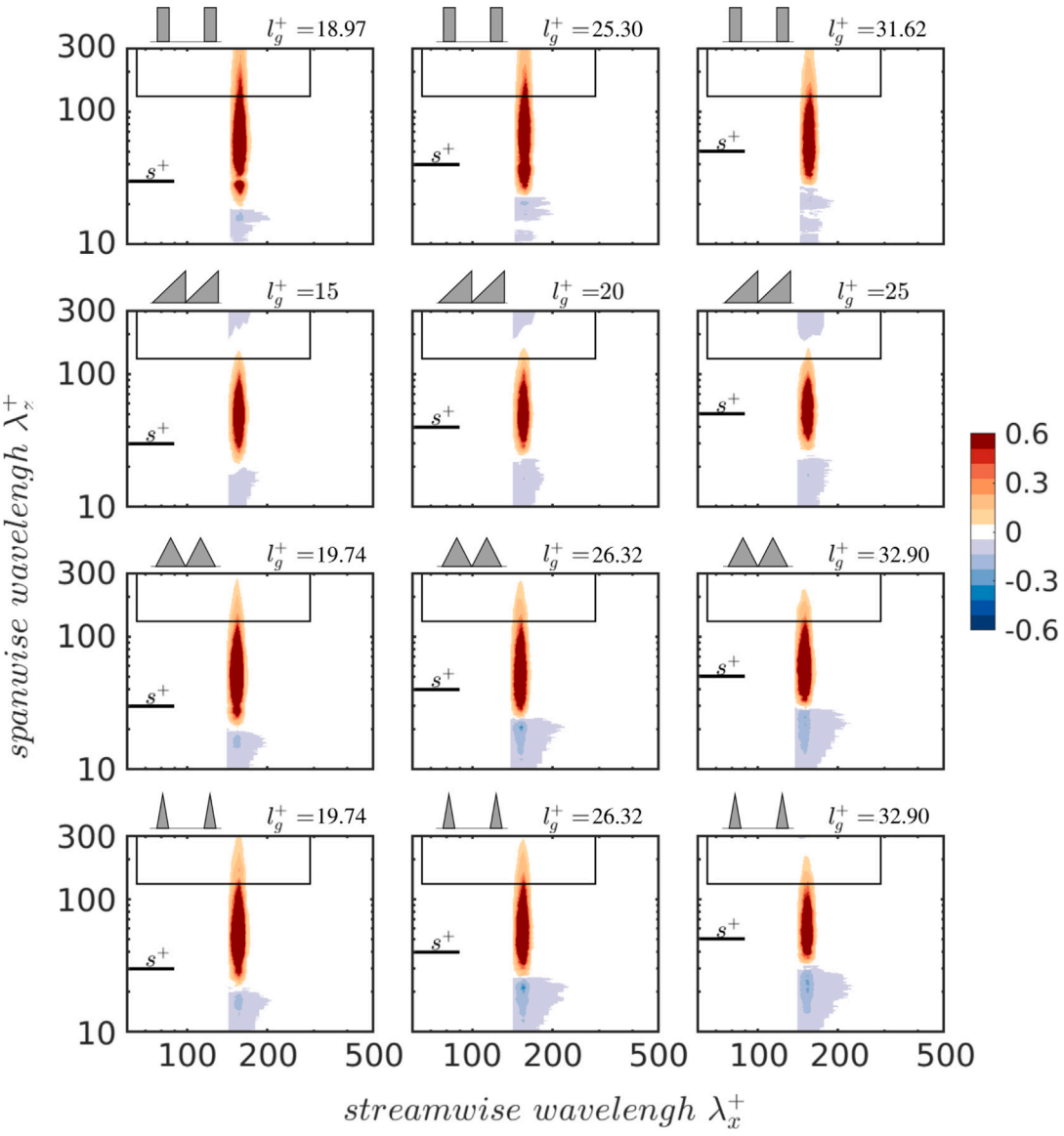

Fig. 10. Premultiplied co-spectra of the Reynolds stress, $k_x^+ k_z^+ E_{uv}^+$, of the larger spacings (s^+ = 30, 40, 50) for each type of riblet investigated. The spectra are taken at a plane located 3 wall units above the riblet tips, $y^+ = \ell_T^+ + 3$, and normalized by $\overline{u'v'}^+$.

likely due to the correspondence between the wavelengths associated with the KH structures in García-Mayoral and Jiménez (2011a) and Chavarin and Luhar (2020) and the streamwise wavenumber support of the RNL dynamics. This conjecture is supported by the fact that a model based on a single resolvent mode corresponding to a streamwise wavelength in the same range as those supporting these RNL dynamics was similarly shown to reproduce the emergence of spanwise rollers resembling KH vortices and the observed breakdown with increasing riblet size (Chavarin and Luhar, 2020). The preliminary results in this section suggest that it is not an inability to predict the spanwise KH-like rollers that leads to the differences in RNL versus DNS predictions of the total stresses in the drag increasing regime.

Future work is needed to determine the source of these differences, in particular whether a larger range of structures in the streamwise wavenumber support or the additional nonlinearity in a more comprehensive model such as the augmented RNL framework, introduced in Minnick et al. (2023), is needed to capture these phenomena. Understanding the minimal physics required could provide further insight into the mechanisms underlying riblet induced drag alterations and inform control approaches that can produced similar effects.

8. Conclusions

This work adapts the RNL modeling framework to flow over a wide range of riblet geometries. The results demonstrate that despite restriction of the nonlinear interactions between streamwise varying modes, the rough-wall RNL representation captures the salient characteristics of turbulent flow over riblets. In particular, RNL simulations reproduce roughness function trends associated with riblet induced alterations to skin friction drag as a function of riblet spacing for four common riblet shapes. Secondary motions quantified through the wall-normal velocity and streamwise vorticity are also faithfully represented by the RNL dynamics. A detailed analysis isolating the contribution of the total stresses including the two-dimensional co-spectra of the Reynolds stress indicates that the RNL model captures stresses linked to KH-like rollers and associated with the breakdown of riblet induced drag reduction in certain riblet geometries. Together these results suggest the utility of the RNL framework as a low-order model for investigating the flow over riblets.

The present study is conducted at a moderate Reynolds number (Re_τ = 395), which may limit the direct applicability of the findings

to higher-Re turbulent flows. Ongoing work includes application of the augmented RNL framework, which has shown promise in higher-Re channel flows (Minnick et al., 2023) and has already proven useful in characterizing flow over riblets (Viggiano et al., 2024). As part of those efforts we will exploit the RNL framework to investigate key streamwise scale interactions and the trade-offs between computational complexity and model fidelity in capturing the critical flow mechanisms. The long term goal of such work is to inform related passive and active flow control techniques.

CRediT authorship contribution statement

Xiaowei Zhu: Writing – review & editing, Writing – original draft, Methodology, Formal analysis. **Bianca Viggiano:** Writing – review & editing, Writing – original draft, Methodology, Formal analysis. **Benjamin A. Minnick:** Writing – review & editing, Methodology. **Dennice F. Gayme:** Writing – review & editing, Supervision, Methodology, Conceptualization.

Funding

This work was supported by the Office of Naval Research (ONR) through grant numbers: N000141712649 and N000142012535 and was partially funded by the US National Science Foundation (grant no. 1652244). This work was carried out with resources of the Advanced Research Computing at Hopkins (ARCH) core facility (rockfish.jhu.edu), which was supported by the National Science Foundation (NSF) grant number OAC 1920103.

Declaration of competing interest

The authors declare that they have no known competing financial interests or personal relationships that could have appeared to influence the work reported in this paper.

Acknowledgments

We would like to thank Dr. Daniel Chung, Dr. Ricardo Garcia-Mayoral, Dr. Mitul Luhar and Dr. Christopher Camobreco for their input on methods, as well as for their insights during many discussions over the course of the work. We are also grateful to the Maryland Advanced Research Computing Center (MARCC) and Advanced Research Computing at Hopkins (ARCH) for providing computational resources.

Data availability

All numerical codes used are available on the LESGO Github: https://github.com/lesgo-jhu/lesgo.

References

del Álamo, J.C., Jiménez, J., 2006. Linear energy amplification in turbulent channels. J. Fluid Mech. 559, 205–213.
Anderson, W., Passalacqua, P., Porté-Agel, F., Meneveau, C., 2012. Large-eddy simulation of atmospheric boundary-layer flow over fluvial-like landscapes using a dynamic roughness model. Bound. Layer Meteorol. 144 (2), 263–286.
Bai, K., Meneveau, C., Katz, J., 2012. Near-wake turbulent flow structure and mixing length downstream of a fractal tree. Bound. Layer Meteorol. 143, 285–308.
Bechert, D.W., Bartenwerfer, M., 1989. The viscous flow on surfaces with longitudinal ribs. J. Fluid Mech. 206, 105–129.
Bechert, D.W., Bruse, M., Hage, W., 2000. Experiments with three-dimensional riblets as an idealized model of shark skin. Exp. Fluids 28 (5), 403–412.
Bechert, D.W., Bruse, M., Hage, W.V., Van der Hoeven, J.T., Hoppe, G., 1997. Experiments on drag-reducing surfaces and their optimization with an adjustable geometry. J. Fluid Mech. 338, 59–87.
Boomsma, A., Sotiropoulos, F., 2016. Direct numerical simulation of sharkskin denticles in turbulent channel flow. Phys. Fluids 28 (3), 035106.
Bretheim, J.U., Meneveau, C., Gayme, D.F., 2015. Standard logarithmic mean velocity distribution in a band-limited restricted nonlinear model of turbulent flow in a half-channel. Phys. Fluids 27 (1), 011702.
Bretheim, J.U., Meneveau, C., Gayme, D.F., 2018. The restricted nonlinear large eddy simulation approach to reduced-order wind farm modeling. J. Renew. Sustain. Energy 10 (4), 043307.
Chavarin, A., Luhar, M., 2020. Resolvent analysis for turbulent channel flow with riblets. AIAA J. 58 (2), 589–599.
Cheng, W.-C., Porté-Agel, F., 2015. Adjustment of turbulent boundary-layer flow to idealized urban surfaces: a large-eddy simulation study. Bound. Layer Meteorol. 155 (2), 249–270.
Chester, S., Meneveau, C., Parlange, M.B., 2007. Modeling turbulent flow over fractal trees with renormalized numerical simulation. J. Comput. Phys. 225 (1), 427–448.
Choi, H., Moin, P., Kim, J., 1993. Direct numerical simulation of turbulent flow over riblets. J. Fluid Mech. 255, 503–539.
Chung, D., Chan, L., MacDonald, M., Hutchins, N., Ooi, A., 2015. A fast direct numerical simulation method for characterising hydraulic roughness. J. Fluid Mech. 773, 418–431.
Chung, D., Monty, J.P., Hutchins, N., 2018. Similarity and structure of wall turbulence with lateral wall shear stress variations. J. Fluid Mech. 847, 591–613.
Cossu, C., Pujals, G., Depardon, S., 2009. Optimal transient growth and very-large-scale structures in turbulent boundary layers. J. Fluid Mech. 619, 79–94.
Endrikat, S., Modesti, D., García-Mayoral, R., Hutchins, N., Chung, D., 2018. Kelvin–Helmholtz rollers in turbulent flow over riblets. In: Proceedings of 21st Australasian Fluid Mechanics Conference.
Endrikat, S., Modesti, D., García-Mayoral, R., Hutchins, N., Chung, D., 2021. Influence of riblet shapes on the occurrence of Kelvin–Helmholtz rollers. J. Fluid Mech. 913.
Fang, J., Porté-Agel, F., 2016. Intercomparison of terrain-following coordinate transformation and immersed boundary methods in large-eddy simulation of wind fields over complex terrain. In: J. Phys. Conf. Ser.. Vol. 753, IOP Publishing, 082008.
Farrell, B.F., Ioannou, P.J., 1993. Stochastic forcing of the linearized Navier–Stokes equations. Phys. Fluids A 5 (11), 2600–2609.
Farrell, B.F., Ioannou, P.J., 2012. Dynamics of streamwise rolls and streaks in turbulent wall-bounded shear flow. J. Fluid Mech. 708, 149–196.
Farrell, B.F., Ioannou, P.J., 2017. Statistical state dynamics-based analysis of the physical mechanisms sustaining and regulating turbulence in Couette flow. Phys. Rev. Fluids 2, 084608.
Farrell, B.F., Ioannou, P.J., Jiménez, J., Constantinou, N.C., Lozano-Durán, A., Nikolaidis, M.-A., 2016. A statistical state dynamics-based study of the structure and mechanism of large-scale motions in plane poiseuille flow. J. Fluid Mech. 809, 290–315.
Flack, K.A., Schultz, M.P., 2010. Review of hydraulic roughness scales in the fully rough regime. J. Fluids Eng. 132 (4).
Flack, K.A., Schultz, M.P., Connelly, J.S., 2007. Examination of a critical roughness height for outer layer similarity. Phys. Fluids 19 (9), 095104.
Flores, O., Jiménez, J., 2010. Hierarchy of minimal flow units in the logarithmic layer. Phys. Fluids 22 (7), 071704.
García-Mayoral, R., Jiménez, J., 2011a. Drag reduction by riblets. Philos. Trans. R. Soc. Lond. Ser. A 369 (1940), 1412–1427.
García-Mayoral, R., Jiménez, J., 2011b. Hydrodynamic stability and breakdown of the viscous regime over riblets. J. Fluid Mech. 678, 317.
García-Mayoral, R., Jiménez, J., 2012. Scaling of turbulent structures in riblet channels up to $Re_\tau = 550$. Phys. Fluids 24 (10), 105101.
Garcia-Mayoral, R., Gómez-de Segura, G., Fairhall, C.T., 2019. The control of near-wall turbulence through surface texturing. Fluid Dyn. Res. 51 (1), 011410.
Gayme, D.F., McKeon, B.J., Bamieh, B., Papachristodoulou, A., Doyle, J.C., 2011. Amplification and nonlinear mechanisms in plane Couette flow. Phys. Fluids 23 (6), 065108.
Gayme, D.F., Minnick, B.A., 2019. Coherent structure-based approach to modeling wall turbulence. Phys. Rev. Fluids 4 (11), 110505.
Giometto, M.G., Christen, A., Meneveau, C., Fang, J., Krafczyk, M., Parlange, M.B., 2016. Spatial characteristics of roughness sublayer mean flow and turbulence over a realistic urban surface. Bound. Layer Meteorol. 160 (3), 425–452.
Goldstein, D., Handler, R., Sirovich, L., 1995. Direct numerical simulation of turbulent flow over a modeled riblet covered surface. J. Fluid Mech. 302, 333–376.
Goldstein, D.B., Tuan, T.C., 1998. Secondary flow induced by riblets. J. Fluid Mech. 363, 115–151.
Guala, M., Hommema, S.E., Adrian, R.J., 2006. Large-scale and very-large-scale motions in turbulent pipe flow. J. Fluid Mech. 554, 521–542.
Hutchins, N., Marusic, I., 2007. Evidence of very long meandering features in the logarithmic region of turbulent boundary layers. J. Fluid Mech. 579, 1–28.
Hwang, Y., 2013. Near-wall turbulent fluctuations in the absence of wide outer motions. J. Fluid Mech. 723, 264–288.
Hwang, Y., Cossu, C., 2010. Linear non-normal energy amplification of harmonic and stochastic forcing in the turbulent channel flow. J. Fluid Mech. 664, 51–73.
Jelly, T.O., Jung, S.Y., Zaki, T.A., 2014. Turbulence and skin friction modification in channel flow with streamwise-aligned superhydrophobic surface texture. Phys. Fluids 26 (9), 095102.
JHU-LESGO, 2019. LESGO: A parallel pseudo-spectral large-eddy simulation code. https://lesgo.me.jhu.edu.

Jiménez, J., Moin, P., 1991. The minimal flow unit in near-wall turbulence. J. Fluid Mech. 225, 213–240.
Jo, S., Ahn, H., Jung, C.M., Song, S., Kim, D.R., 2018. Water-repellent hybrid nanowire and micro-scale denticle structures on flexible substrates of effective air retention. Sci. Rep. 8 (1), 1–10.
Jovanović, M.R., Bamieh, B., 2005. Componentwise energy amplification in channel flows. J. Fluid Mech. 534, 145–183.
Kim, K.C., Adrian, R.J., 1999. Very large-scale motion in the outer layer. Phys. Fluids 11 (2), 417–422.
Kramer, M., 1937. Einrichtung zur verminderurg des reibungswide stands (Device for reducing the frictional resistance). Ger. Pat. (669897).
Lee, S.J., Lee, S.H., 2001. Flow field analysis of a turbulent boundary layer over a riblet surface. Exp. Fluids 30 (2), 153–166.
Lee, M., Moser, R.D., 2015. Direct numerical simulation of turbulent channel flow up to Re_τ=5200. J. Fluid Mech. 774, 395–415.
Li, Q., Bou-Zeid, E., Anderson, W., 2016. The impact and treatment of the Gibbs phenomenon in immersed boundary method simulations of momentum and scalar transport. J. Comput. Phys. 310, 237–251.
Luchini, P., Manzo, F., Pozzi, A., 1991. Resistance of a grooved surface to parallel flow and cross-flow. J. Fluid Mech. 228, 87–109.
MacDonald, M., Chung, D., Hutchins, N., Chan, L., Ooi, A., García-Mayoral, R., 2017. The minimal-span channel for rough-wall turbulent flows. J. Fluid Mech. 816, 5–42.
Marusic, I., 2001. On the role of large-scale structures in wall turbulence. Phys. Fluids 13 (3), 735–743.
McKeon, B.J., Sharma, A.S., 2010. A critical-layer framework for turbulent pipe flow. J. Fluid Mech. 658, 336–382.
Meinhart, C.D., Adrian, R.J., 1995. On the existence of uniform momentum zones in a turbulent boundary layer. Phys. Fluids 7 (4), 694–696.
Minnick, B.A., Gayme, D.F., 2019. Characterizing energy transfer in restricted nonlinear wall-bounded turbulence. In: Proceedings of 11th International Symposium on Turbulence and Shear Flow Phenomena.
Minnick, B., Viggiano, B., Gayme, D., 2023. Augmented restricted nonlinear (ARNL) model for high Reynolds number wall-turbulence. In: Conference on Interdisciplinary Turbulence Initiative. Springer, pp. 65–75.
Modesti, D., Endrikat, S., Garcıa-Mayoral, R., Hutchins, N., Chung, D., 2018. Form-induced stress in turbulent flow over riblets. In: Proceedings of 21st Australasian Fluid Mechanics Conference.
Modesti, D., Endrikat, S., García-Mayoral, R., Hutchins, N., Chung, D., 2019. Contribution of dispersive stress to skin friction drag in turbulent flow over riblets. In: Proceedings of 11th International Symposium on Turbulence and Shear Flow Phenomena.
Modesti, D., Endrikat, S., Hutchins, N., Chung, D., 2021. Dispersive stresses in turbulent flow over riblets. J. Fluid Mech. 917.
Monty, J.P., Stewart, J.A., Williams, R.C., Chong, M.S., 2007. Large-scale features in turbulent pipe and channel flows. J. Fluid Mech. 589, 147–156.
Moser, R.D., Kim, J., Mansour, N.N., 1999. Direct numerical simulation of turbulent channel flow up to Re_τ= 590. Phys. Fluids 11 (4), 943–945.
Newton, R., Chung, D., Hutchins, N., 2018. An experimental investigation into the breakdown of riblet drag reduction at post-optimal conditions. In: 21st Australasian Fluid Mechanics Conference, Adelaide, Australia.
Peskin, C.S., 2002. The immersed boundary method. Acta Numer. 11, 479–517.
Pope, S.B., 2001. Turbulent Flows. IOP Publishing.
Prandtl, L., 1931. Einführung in die Grundbegriffe der Strömungslehre. Akademische Verlagsgesellschaft.
Raayai-Ardakani, S., McKinley, G.H., 2017. Drag reduction using wrinkled surfaces in high Reynolds number laminar boundary layer flows. Phys. Fluids 29 (9), 093605.
Ran, W., Zare, A., Jovanović, M.R., 2021. Model-based design of riblets for turbulent drag reduction. J. Fluid Mech. 906.
Reddy, S.C., Ioannou, P.J., 2000. Energy transfer analysis of turbulent plane couette flow. In: Laminar-Turbulent Transition: IUTAM Symposium, Sedona/AZ September 13–17, 1999. Springer, pp. 211–216.
Rouhi, A., Endrikat, S., Modesti, D., Sandberg, R.D., Oda, T., Tanimoto, K., Hutchins, N., Chung, D., 2022. Riblet-generated flow mechanisms that lead to local breaking of Reynolds analogy. J. Fluid Mech. 951, A45.
Schultz, M., Flack, K., 2005. Outer layer similarity in fully rough turbulent boundary layers. Exp. Fluids 38, 328–340.
Gómez-de Segura, G., García-Mayoral, R., 2019. Turbulent drag reduction by anisotropic permeable substrates – analysis and direct numerical simulations. J. Fluid Mech. 875, 124–172.
Smits, A.J., McKeon, B.J., Marusic, I., 2011. High-Reynolds number wall turbulence. Annu. Rev. Fluid Mech. 43 (1), 353–375.
Thomas, V., Farrell, B., Ioannou, P., Gayme, D.F., 2015. A minimal model of self-sustaining turbulence. Phys. Fluids 27, 105104.
Thomas, V.L., Lieu, B.K., Jovanović, M.R., Farrell, B.F., Ioannou, P.J., Gayme, D.F., 2014. Self-sustaining turbulence in a restricted nonlinear model of plane couette flow. Phys. Fluids 26 (10), 105112.
Townsend, A.A.R., 1980. The Structure of Turbulent Shear Flow. Cambridge University Press.
Viggiano, B., Camobreco, C., Wong, J., Luhar, M., García-Mayoral, R., Chung, D., Gayme, D., 2024. The role of nonlinear interactions in the onset of drag increase in flow over riblets. In: J. Phys. Conf. Ser.. Vol. 2753, IOP Publishing, 012010.
Walsh, M., 1980. Drag characteristics of V-groove and transverse curvature riblets. In: Symposium on Viscous Flow Drag Reduction.
Walsh, M., 1982. Turbulent boundary layer drag reduction using riblets. In: Proceedings of 20th Aerospace Sciences Meeting. p. 169.
Walsh, M., Lindemann, A., 1984. Optimization and application of riblets for turbulent drag reduction. In: Proceedings of 22nd Aerospace Sciences Meeting. p. 347.
Wang, M., Wang, Q., Zaki, T.A., 2019. Discrete adjoint of fractional-step incompressible Navier-Stokes solver in curvilinear coordinates and application to data assimilation. J. Comput. Phys. 396, 427–450.
Wen, S., Wang, W., Wu, S., 2020. Drag reduction by various micro-grooves in a rotating disk system. P. I. Mech. Eng. A - J. Pow. 234 (1), 110–123.
Wong, J., Camobreco, C., García-Mayoral, R., Hutchins, N., Chung, D., 2024. A viscous vortex model for predicting the drag reduction of riblet surfaces. J. Fluid Mech. 978, A18.
Yang, X., Meneveau, C., 2016. Large eddy simulations and parameterisation of roughness element orientation and flow direction effects in rough wall boundary layers. J. Turbul. 17 (11), 1072–1085.
Zheng, X.F., Yan, Y.Y., 2010. A biomimetic smart control of viscous drag reduction. Adv. Nat. Sci. 3 (2), 139–151.